Experimental parametric subharmonic instability in stratified fluids

Sylvain Joubaud,[1,a)] James Munroe,[2,b)] Philippe Odier,[1,c)] and Thierry Dauxois[1,d)]
[1]*Laboratoire de Physique de l'École Normale Supérieure de Lyon, CNRS and Université de Lyon, 46 Allée d'Italie, 69007 Lyon, France*
[2]*Department of Physics and Physical Oceanography, Memorial University of Newfoundland, St. John's, NL A1B 3X7, Canada*

(Received 11 January 2012; accepted 24 March 2012; published online 27 April 2012)

Internal gravity waves contribute to fluid mixing and energy transport, not only in oceans but also in the atmosphere and in astrophysical bodies. An efficient way to transfer energy from large scale to smaller scale is the parametric subharmonic instability. We provide here the first experimental measurement of the growth rate of this instability. We make careful and quantitative comparisons with theoretical predictions for propagating vertical modes in laboratory experiments. © *2012 American Institute of Physics*. [http://dx.doi.org/10.1063/1.4706183]

Internal gravity waves result from the balance of inertia and buoyancy forces in a density stratified fluid. Such waves have received a great deal of attention recently because of their relevance and ubiquity in different physical situations: they are believed to be of primary importance as they affect ocean mixing and energy transport.[1] Although internal gravity waves do not play the dominant role in the evolution of weather and climate, their influence is non-negligible in the dynamics of the atmosphere.[2] From a fundamental point of view, these waves are also particularly intriguing. A striking consequence of stratification is an anisotropic dispersion relation relating the frequency to the direction of propagation of the wave and not to the wavelength. This property is also encountered for inertial waves (in presence of rotation) or plasma waves (in presence of a magnetic field). This has unexpected and interesting consequences in the propagation, reflection,[3] or transmission properties of these waves.[4]

Internal waves are known to be inherently unstable due to parametric subharmonic instability (PSI).[5] PSI is a type of resonant triad interaction where nonlinear terms in the equations of motion allow for efficient transfer of energy from large to small length scales where it can be dissipated. The terminology "parametric subharmonic" is used because, for inviscid fluids, PSI transfers energy from a primary wave to two recipient waves of half the frequency. As viscosity effects set in, the frequencies of the recipient waves diverge from half the frequency of the primary wave. In previous laboratory experiments, PSI has been qualitatively observed by driving low-order standing modes with plungers on the sides of the container,[6] with an oscillating paddle[7,8] or relying on the parametric forcing of the tank.[9] For large amplitude forcing, "irregularities" or "traumata" were observed, which led to mixing and overturning. In Ref. 8, the critical amplitude of the instability has been measured. Quantitative measurements of the growth rate of the instability have never been reported.

We present here experiments performed with a wave generator, which produces sinusoidal vertical modes propagating along a rectangular tank. We measured the growth rate of the instability. This quantity is of paramount importance to single out the major mechanism in dissipation processes,

[a)]Electronic mail: sylvain.joubaud@ens-lyon.fr.
[b)]Electronic mail: jmunroe@mun.ca.
[c)]Electronic mail: philippe.odier@ens-lyon.fr.
[d)]Electronic mail: thierry.dauxois@ens-lyon.fr.

a recently highly debated issue.[1,10,11] We first briefly outline theoretical aspects of this instability, after which the experimental configuration is described. Then we present our experimental results and compare some of them with theoretical predictions.

Internal waves are characterized by the buoyancy frequency, $N = \sqrt{(-g/\bar{\rho}_0)(\mathrm{d}\rho_0/\mathrm{d}z)}$, in which g is the acceleration of gravity, $\bar{\rho}_0$ is the characteristic fluid density, and $(\mathrm{d}\rho_0/\mathrm{d}z)$ is the density gradient in the vertical direction z. At large Prandtl number, the 2D Boussinesq equations of motion can be written as

$$\frac{\partial^2 \nabla^2 \psi}{\partial t^2} + N^2 \frac{\partial^2 \psi}{\partial x^2} = \frac{\partial}{\partial t} J(\psi, \nabla^2 \psi) - \frac{g}{\rho_0} \frac{\partial}{\partial x} J(\tilde{\rho}, \psi) + \nu \nabla^4 \psi_t \,, \tag{1}$$

where $\tilde{\rho} = \rho - \rho_0$ is the perturbation density field, ψ is the stream function, J is the Jacobian operator, and ν is the viscosity. Seeking wave solutions with wave number $\vec{k} = (k, m)$, Eq. (1) leads to the inviscid linear dispersion relation for frequency ω,

$$\omega^2 = N^2 \frac{k^2}{k^2 + m^2}. \tag{2}$$

For small amplitudes, it can be assumed that several waves concurrently exist simply as a linear superposition. In the case of a resonant triad interaction, where three waves satisfy the spatial resonance condition

$$\vec{k_0} = \vec{k_1} + \vec{k_2} \,, \tag{3}$$

and the temporal resonance condition

$$\omega_0 = \omega_1 + \omega_2 \,, \tag{4}$$

the nonlinear terms of Eq. (1) act as forcing terms transferring energy between the three waves. Each wave must satisfy the dispersion relation (2). A finite amplitude, large length scale, high frequency wave $(\vec{k_0}, \omega_0)$ can transfer energy to produce two secondary waves of smaller length scales and lower frequencies, $(\vec{k_1}, \omega_1)$ and $(\vec{k_2}, \omega_2)$. The instability results from a competition between nonlinear effects and viscous dissipation. The growth is exponential if the amplitude of the secondary waves is initially small compared to the amplitude of the primary wave.[12,13] In this case, the growth rate is equal to

$$\lambda = -\frac{1}{2}(T_1 + T_2) + \left[\frac{1}{4}(T_1 - T_2)^2 + I_1 I_2 \psi_0^2\right]^{1/2}, \tag{5}$$

where ψ_0 is the amplitude of the stream function of the primary wave, I_1 and I_2 are the interaction coefficients

$$I_i = \frac{k_p m_q - k_q m_p}{2\omega_i \kappa_i^2} \left[\omega_i(\kappa_p^2 - \kappa_q^2) + N^2 k_i \left(\frac{k_p}{\omega_p} - \frac{k_q}{\omega_q}\right)\right], \tag{6}$$

and i, p, $q = 0$, 1, or 2 while $T_i = \nu \kappa_i^2/2$ is the viscous damping factor of the wave i and $\kappa^2 = k^2 + m^2$.

A tank, 160 cm long and 17 cm wide, is filled with linearly stratified salt water with constant buoyancy frequency N using the standard double bucket method. A monochromatic vertical mode-1 wave is generated using the wave generator employed in previous experiments.[14,15] The generator is composed of 50 plates moving horizontally to impose the horizontal velocity component of a mode-1, i.e., $u(x = 0, z, t) = -a\omega_0 \cos(\pi z/H)\cos(\omega_0 t)$, H being the water depth, ω_0 being the excitation frequency, and a being the amplitude of the oscillation of the plates. The motion of the fluid is captured by the synthetic schlieren technique using a dotted image behind the tank.[16] A camera is used to acquire images of this background at 1.875 frames/s. The CIVx algorithm[17] computes the cross correlation between the real-time and the $t = 0$ background images, giving the variation of the horizontal, $\tilde{\rho}_x(x, z, t) = \partial_x(\rho(x, z, t) - \rho_0(z))$, and vertical, $\tilde{\rho}_z(x, z, t) = \partial_z(\rho(x, z, t) - \rho_0(z))$, density gradients.

Snapshots of an experimental horizontal density gradient field at different times for a particular experiment are presented in Fig. 1. At early times, a pure vertical mode-1 wave can be seen

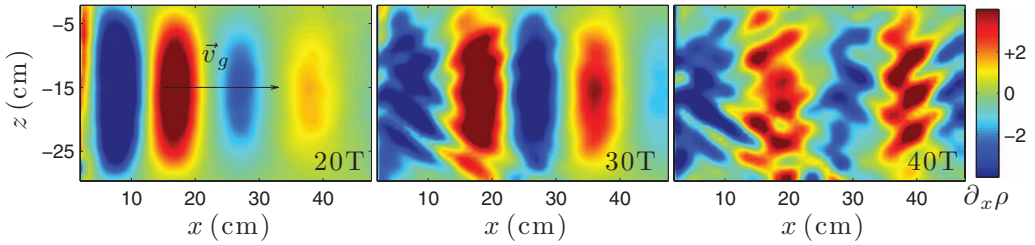

FIG. 1. Snapshots of the horizontal density gradient (in kg m^{-4}) obtained at $t = 20T$, $t = 30T$, and $t = 40T$ with the parameters $a = 0.5$ cm, $\omega_0 = 0.95N$, and $N = 0.822$ rad s^{-1}. On the left-hand panel the direction of the group velocity, $\vec{v}_g$, is indicated. After $20T$, the primary wave has only reached a steady state in the first 20 cm from the generator (see Fig. 4).

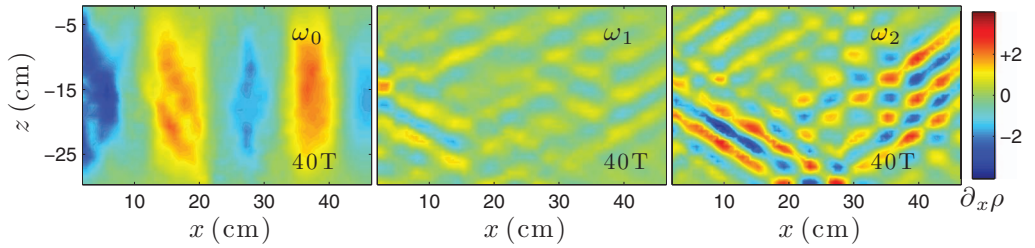

FIG. 2. Real part of the Hilbert transform of $\tilde{\rho}_x$ at $t = 40T$ (see Fig. 1 (right)) presented after filtering at $\omega_0 = 0.95N$ (left), $\omega_1 = 0.38N$ (center), and $\omega_2 = 0.57N$ (right). Note that the shade scale (color scale) is the same as in Fig. 1.

propagating to the right away from the wave generator located at $x = 0$: this is the *primary wave.* After several frequency periods T (typically 30), this wave is destabilized and two *secondary waves* appear, with different frequencies and wave numbers from the primary wave. To see these waves more clearly, the horizontal density gradient at later times is filtered at the frequency of the primary wave ω_0 and at the frequencies of the two secondary waves ω_1 and ω_2. As described below, the frequencies ω_1 and ω_2 were determined from a power spectrum. The result is shown in Fig. 2. Some of the energy of the primary wave has been transferred to both secondary waves, leading to a decrease in the amplitude of the primary wave (compare the left part of Fig. 1 (left) and Fig. 2 (left)). These two waves have smaller frequency and also smaller wavelength. In agreement with the dispersion relation, which links the frequency to the angle of propagation of the wave, the angle of constant phase is different for the two wavelengths. For the experiment presented in Fig. 1, the three measured frequencies $(\omega_0, \omega_1, \omega_2)$ are equal to $(0.95, 0.38, 0.57)N$, attesting that the temporal resonance condition (4) is satisfied. To justify that the spatial resonance condition (3) is also satisfied, the components of the three wavevectors have to be measured. This is done by extracting the phase of the signal at a given frequency, $\omega_{0,1,2}t \pm k_{0,1,2}x \pm m_{0,1,2}z$, using a Hilbert transform.[18] At a fixed time and x (respectively, z), the phase is linear with the position z (resp. x). The component $m_{0,1,2}$ (resp. $k_{0,1,2}$) is given by the slope of the linear fit. Within experimental errors, the wave vectors, represented in Fig. 3, satisfy the theoretical spatial resonance condition (3).

The measured density gradient fields are then analyzed using a time-frequency representation calculated at each spatial point

$$S_x(t, \omega) = \left| \int_{-\infty}^{+\infty} \mathrm{d}u \, \tilde{\rho}_x(u) \, e^{i\omega u} \, h(t - u) \right|^2 , \tag{7}$$

where h is a smoothing Hamming window of energy unity.[19] Good frequency resolution is provided by a large time window h while good time resolution is provided by small time window h. To increase the signal to noise ratio, the data is averaged along a vertical line over the water depth. For large ω_0/N values, the dissipation length is small, so the analysis line is chosen to be close to the generator so that the amplitude is large.

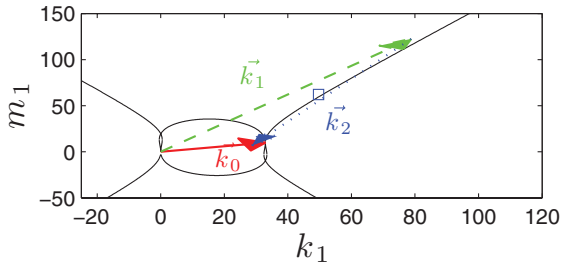

FIG. 3. Spatial resonance conditions for the experiment presented in Fig. 1. The black line represents the theoretical location of the tip of the wave vector $\vec{k_1}$ for a given primary wave vector $\vec{k_0}$ so that the resonance conditions (3) and (4) and dispersion relations (2) are satisfied. The three arrows are the experimental measurement of the three wave vectors: the solid arrow (red) is the primary wave vector $\vec{k_0}$, the dashed (green) and the dotted (blue) arrows are the secondary wave vectors $\vec{k_1}$ and $\vec{k_2}$. The square □ represents the most unstable theoretical mode.

Figure 4 (left) presents the spectra of the density field for four different excitation amplitudes with $\omega_0 = 0.94N$. The spectra are obtained using a time window width equal to 100 T to have good frequency resolution. $S_x(t, \omega)$ is then averaged over the 10 last periods. Analyzing first the result for the amplitude 0.5 cm, the picture emphasizes a large peak close to N, corresponding to the frequency of the mode-1 wave. A pair of twin peaks is observed, corresponding to secondary waves of frequencies, ω_1 and ω_2, smaller than ω_0.

The amplitude of each wave is then computed using a time-frequency analysis with a time window width equal to 20 T to increase time resolution. The amplitude of the secondary wave of frequency ω_1 is presented in Fig. 4 (right). After several forcing periods, a steady state for the primary wave is reached. After a time interval, the secondary wave starts to grow and a linear increase of the amplitude on a semilogarithmic plot is observed, confirming exponential growth. The value of the growth rate λ is measured using a linear fit, shown with the dashed lines in Fig. 4 (right). The amplitude of the secondary waves eventually saturates.

Comparing the different curves in Fig. 4, one observes that the amplitude has an influence not only on the location but also on the height of the peaks of the secondary waves in the spectrum. If the amplitude of the primary wave is too small, no peaks are visible and therefore no instability is observed during the experiment run time, T_{run}. This result shows that the growth rate in this particular case has to be smaller than $1/T_{\text{run}}$. It may also give an indication of the existence of a threshold in amplitude. As the amplitude increases, the distance between the two peaks increases and the

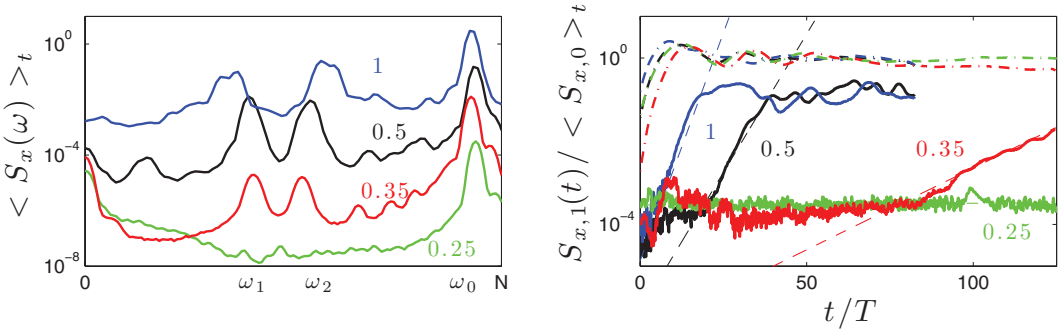

FIG. 4. (Left) Spectra of the density gradient field, $\langle S_x(\omega)\rangle_t$, for four different excitation amplitudes for $\omega_0 = 0.94N$ measured at $x \approx 12$ cm. The amplitudes are, respectively, 0.25 cm (green), 0.35 (red), 0.5 (black), and 1 (blue). The value of the amplitude is indicated next to the corresponding curve. The spectra 0.25, 0.35, and 1 are multiplied, respectively, by 0.01, 0.1, and 10 for illustration purposes. (Right) Amplitude of the secondary wave ω_1, $S_{x,1}(t)$, normalized by the amplitude of the primary wave, $\langle S_{x,0}\rangle_t$, averaged over time when the steady state of the mode-1 has been reached. Results are similar for the other secondary wave ω_2. The dashed-dotted lines represent the amplitude of the primary wave using the same normalization. The dashed lines show the linear fit, which gives the value of the growth rate λ.

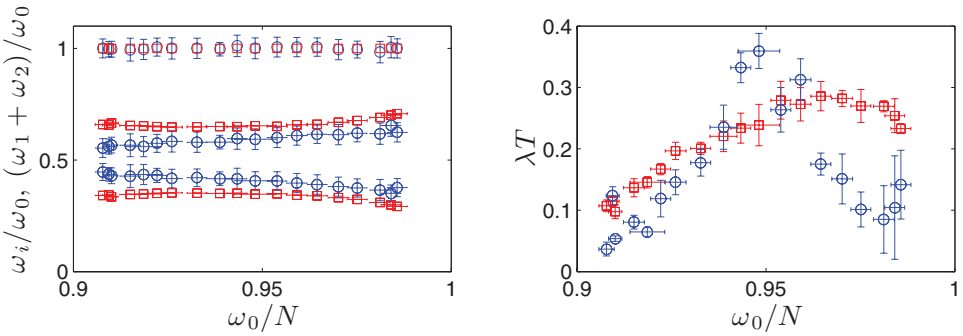

FIG. 5. (Left) Values of the frequencies of the secondary waves for the experiments (○, blue) and the theoretical calculation (□, red). The vertical and horizontal error bars are defined as the half-width of the corresponding peak. The top line of point corresponds to the sum of the frequencies, with corresponding symbols for theoretical and experimental data. (Right) Values of the growth rate of the secondary waves for the experiments (○, blue) and the theoretical calculation (□, red). Vertical error bars for the experimental results come from the choice of the horizontal location and from the linear fit. T is the period of the primary wave. The theoretical values (□, red) are computed using Eq. (5) and the measured amplitude of the primary wave. The vertical error bars come from the error made measuring the amplitude of the mode-1.

instability occurs earlier (after fewer forcing periods) and is stronger, i.e., with a larger growth rate, which is in agreement with the theoretical growth rate (5).

Experiments were performed using the same stratification and an amplitude of 0.5 cm for frequencies in the range of $0.9 < \omega_0/N < 1$. For each experiment, the value of the frequencies of the two secondary waves, ω_1 and ω_2, and the growth rate λ were measured. Experimental results are presented as a function of the frequency of the primary wave, ω_0/N, in Fig. 5. The sum of the frequencies of the two secondary waves, $\omega_1 + \omega_2$, is equal to the frequency of the primary wave, ω_0, within experimental errors, in agreement with Eq. (4). As ω_0/N increases, the distance between the two secondary frequencies is larger. The measured value of the growth rate is presented in Fig. 5 (right). The growth rate increases to reach a maximum around $\omega_0 = 0.95N$ and then decreases as ω_0 gets closer to N.

To compare quantitatively the experimental results with the theoretical prediction of the growth rate, the value of the amplitude of the mode-1 wave has to be precisely known. The theoretical value of the amplitude of the streamfunction is equal to $a\omega_0/m_0$. However, the conversion efficiency from the energy of the wavemaker to the energy of the mode-1 is less than unity and depends on experimental conditions.[15] Moreover, as ω_0 gets closer to the cut-off frequency, N, the value of the viscous damping increases.[20] Consequently, the efficiency is not the same for all primary frequencies ω_0, and the amplitude of the primary wave has to be measured experimentally to compute the theoretical value of the growth rate. It is important to check that the steady state of the mode-1 wave has been reached. However, the tank being finite in length, the measurement has to be performed before the mode-1 wave reflects back into the measurement area. Then, using a linear polarization relation, the amplitude ψ_0 of the stream function at this particular frequency and wave number is $\psi_0 = g\omega_0\partial_x\tilde{\rho}_0/(4k_0^2\bar{\rho}N^2)$. The theoretical frequency pair (ω_1, ω_2) of the instability is defined as the one that maximizes the growth rate. Without adjustable parameters, the comparison between experimental and theoretical results, presented in Fig. 5, emphasizes a good quantitative agreement.

We have reported the first experimental measurement of the growth rate of parametric subharmonic instability in stratified fluids and we have demonstrated this effect in a systematic set of laboratory experiments allowing careful comparisons with theoretical predictions. In practice, this heavily debated mechanism[10] has implications for many geophysical scenarios. Interestingly, although the generation mechanisms of oceanic internal gravity waves are quite well understood, the comprehension of the processes by which they dissipate is much more open. Consequently, determining the relative importance of parametric subharmonic instability, among the four recognized dissipation processes,[1] is the next step in furthering our understanding of how internal waves impact

ocean mixing. Quantitative measurements of the subsequent mixing together with a fundamental study of wave turbulence would be of high interest.

The authors thank G. Bordes, P. Borgnat, B. Bourget, and C. Staquet, for helpful discussions. This work has been partially supported by the PIWO grant (ANR-08-BLAN-0113-01) and the ONLITUR grant (ANR-2011-BS04-006-01). This work has been partially achieved thanks to the resources of PSMN (Pôle Scientifique de Modélisation Numérique) de l'ENS de Lyon.

[1] E. Kunze and S. G. L. Smith, "The role of small scale topography in turbulent mixing of the global ocean," Oceanography **17**, 55 (2004).
[2] B. Sutherland, *Internal Gravity Waves* (Cambridge University Press, London, 2011).
[3] H. P. Zhang, B. King, and H. L. Swinney, "Resonant generation of internal waves on a model continental slope," Phys. Rev. Lett. **100**, 244504 (2008).
[4] M. Mathur and T. Peacock, "Internal wave interferometry," Phys. Rev. Lett. **104**, 118501 (2010).
[5] C. Staquet and J. Sommeria, "Internal gravity waves: From instabilities to turbulence," Annu. Rev. Fluid Mech. **34**, 559 (2002).
[6] S. Thorpe, "On standing internal gravity waves of finite amplitude," J. Fluid Mech. **32**, 489 (1968).
[7] A. McEwan, "Degeneration of resonantly-excited standing internal gravity waves," J. Fluid Mech. **50**, 431 (1971).
[8] A. D. McEwan, D. W. Mander, and R. K. Smith, "Forced resonant second-order interaction between damped internal waves," J. Fluid Mech. **55**, 589 (1972).
[9] D. Benielli and J. Sommeria, "Excitation and breaking of internal gravity waves by parametric instability," J. Fluid Mech. **374**, 117 (1998).
[10] D. Olbers and N. Pomphrey, "Disqualifying two candidates for the energy-balance of oceanic internal waves," J. Phys. Oceanogr. **11**, 1423 (1981).
[11] J. MacKinnon and K. Winters, "Subtropical catastrophe: Significant loss of low-mode tidal energy at 28.9 degrees," Geophys. Res. Lett. **32**, L15605, doi:10.1029/2005GL023376 (2005).
[12] C. Koudella and C. Staquet, "Instability mechanisms of a two-dimensional progressive internal gravity wave," J. Fluid Mech. **548**, 165 (2006).
[13] A. D. McEwan and R. A. Plumb, "Off-resonant amplification of finite internal wave packets," Dyn. Atmos. Oceans **2**, 83 (1977).
[14] L. Gostiaux, H. Didelle, S. Mercier, and T. Dauxois, "A novel internal wave generator," Exp. Fluids **42**, 123 (2007).
[15] M. Mercier, D. Martinand, M. Mathur, L. Gostiaux, T. Peacock, and T. Dauxois, "New wave generation," J. Fluid Mech. **657**, 308 (2010).
[16] S. Dalziel, G. O. Hughes, and B. Sutherland, "Whole-field density measurements by 'synthetic schlieren'," Exp. Fluids **28**, 322 (2000).
[17] A. Fincham and G. Delerce, "Advanced optimization of correlation imaging velocimetry algorithms," Exp. Fluids **29**, S13 (2000).
[18] M. Mercier, N. Garnier, and T. Dauxois, "Reflection and diffraction of internal waves analyzed with the Hilbert transform," Phys. Fluids **20**, 086601 (2008).
[19] P. Flandrin, *Time-Frequency/Time-Scale Analysis* (Academic, San Diego, 1999); see http://tftb.nongnu.org/ for Time-Frequency Toolbox for Matlab©.
[20] P. Echeverri, M. R. Flynn, T. Peacock, and K. B. Winters, "Low-mode internal tide generation by topography: an experimental and numerical investigation," J. Fluid Mech. **636**, 91 (2009).